

# CoRa: A Collision-Resistant LoRa Symbol Detector of Low Complexity

José Álamos  
HAW Hamburg  
jose.alamos@haw-hamburg.de

Thomas C. Schmidt  
HAW Hamburg  
t.schmidt@haw-hamburg.de

Matthias Wählisch  
TU Dresden and Barkhausen Institut  
m.waehlich@tu-dresden.de

**Abstract**—Long range communication with LoRa has become popular as it avoids the complexity of multi-hop communication at low cost and low energy consumption. LoRa is openly accessible, but its packets are particularly vulnerable to collisions due to long time on air in a shared band. This degrades communication performance. Existing techniques for demodulating LoRa symbols under collisions face challenges such as high computational complexity, reliance on accurate symbol boundary information, or error-prone peak detection methods. In this paper, we introduce CoRa, a symbol detector for demodulating LoRa symbols under severe collisions. CoRa employs a Bayesian classifier to accurately identify the true symbol amidst interference from other LoRa transmissions, leveraging empirically derived features from raw symbol data. Evaluations using real-world and simulated packet traces demonstrate that CoRa clearly outperforms the related state-of-the-art, *i.e.*, up to 29% better decoding performance than TnB and 178% better than CIC. Compared to the LoRa baseline demodulator, CoRa magnifies the packet reception rate by up to  $11.53\times$ . CoRa offers a significant reduction in computational complexity compared to existing solutions by only adding a constant overhead to the baseline demodulator, while also eliminating the need for peak detection and accurately identifying colliding frames.

**Index Terms**—LWPAN, LoRa, collision resolution, low power wireless communication

## I. INTRODUCTION

Low Power Wide Area Network (LPWAN) technologies are emerging as a promising solution for the Internet of Things (IoT), as these avoid the complexity of multi-hop communication while maintaining low deployment costs. The inherent characteristics of LPWAN technologies, *i.e.*, long-range communication and low power consumption, make them suitable for a diverse range of IoT use cases, including environmental monitoring, asset tracking, and smart cities. Hence, LPWAN technologies are expected to continuously attract significant interest and investment in the coming years.

LoRa has emerged as a particularly noteworthy solution in both industry and academia due to its flexibility, wide availability, and cost-effectiveness. LoRa can operate in unlicensed spectrum, such as the 868 MHz band in Europe, the 915 MHz band in the United States and the 2.4 GHz band worldwide. It is typically used within the LoRaWAN architecture, which provides a cloud-based MAC layer to facilitate device communication. The LoRa modulation utilizes

a variant of the chirp spread spectrum (CSS) technique, which enables a broad transmission range of several kilometers in urban environments and tens of kilometers in rural areas. This is achieved through the use of a linearly modulated chirp that spreads the transmission over a wide frequency band, resulting in robustness against multipath fading, interference, and the Doppler effect.

Existing studies [1] estimate 42,000 devices per square kilometer in urban deployments, with each device transmitting 100-byte payloads, 300 times per day. In the EU868 region, with 8-channel LoRaWAN gateways, assuming 35% of device employ spreading factor 7 (bandwidth 125 kHz), a gateway covering an 800 m radius would receive about 10 packets per second per channel. Given a 190 ms time-on-air (ToA) for each packet, no more than 5 packets per second can be transmitted without overlap, making collisions unavoidable. While LoRa frames can be decoded if the received signal is stronger than the colliding one (capture effect), collisions of similar power prevent decoding.

Recent work has studied the decoding of LoRa frames under collisions to increase the overall utility and bandwidth of LoRa networks and could demonstrate a significant increase in network capacity. However, these approaches often entail high computational complexity, pose challenges for real-time operation or require a prior knowledge of the position of interference frames relative to the target frame. The latter is ineffective if the frame detection algorithm fails to detect interfering frames, a situation that is common under severe frame collisions or a low Signal-to-Noise Ratio (SNR). These limitations challenge implementability on real-world devices.

In this work, we propose CoRa, an alternative symbol detector designed to accurately classify LoRa symbols by employing a Bayesian classifier. CoRa is specifically engineered to identify the true symbol within a frame amidst interferences in the received signal, all while maintaining low computational complexity. This approach enhances the demodulation accuracy of LoRa symbols in congested environments, leading to a significant improvement in the Packet Reception Ratio (PRR). Our contributions read:

- 1) We design a new detection feature based on waveform symmetries, which arms our Bayesian classifier.
- 2) We demonstrate the ability to accurately demodulate symbols under collisions and under significant channel fluctuations by employing our robust symbol detector.

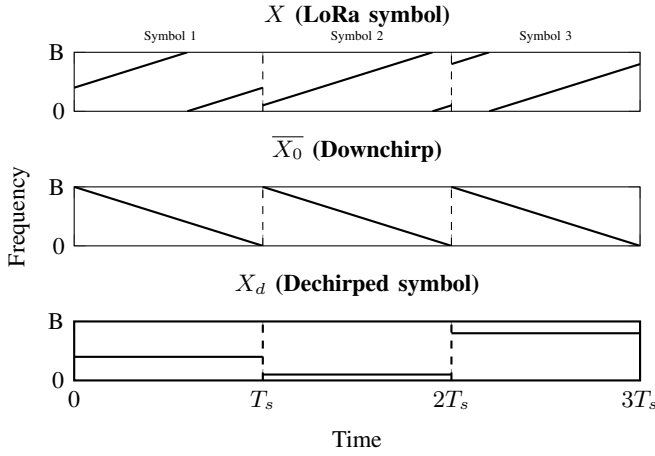


Fig. 1: Spectrogram of a LoRa symbols (top), downchirp signal (middle) and dechirped symbols used for demodulation (bottom).

- 3) By leveraging the current state-of-the-art LoRa decoder (TnB Block Error Correction) in real-world captures, we achieve an improvement of Packet Reception Ratios (PRRs) of up to 29% over the current state-of-the-art and approximately 11.53 times better performance than the baseline LoRa decoder.

The remainder of this paper is structured as follows. Section II provides the necessary background on LoRa transmission along with related work. Section III details the proposed design for the LoRa symbol detector. We present the evaluation on real-world and simulated data in Section IV and a discussion in Section V. Finally, we conclude the paper in Section VI with an outlook on future research.

## II. BACKGROUND AND RELATED WORK

A LoRa symbol  $x(t)$  (Figure 1, top) encodes information by shifting the frequency offset of a linearly modulated complex chirp  $x_0(t) = e^{j(\pi \frac{B}{T_s} t^2)}$  with bandwidth  $B$  and symbol time  $T_s = \frac{2^{SF}}{B}$ , where  $SF$  denotes the spreading factor of the signal. This process transforms the symbol into the form  $x(t) = x_0(t) \cdot e^{j2\pi f_m t}$ , wherein  $f_m$  corresponds to the frequency offset.

The LoRa signal is characterized by the signal circumvolution at the boundary values, analogous to sampling at its Nyquist frequency,  $B$ . This approach provides two benefits: (i) efficient modulation of LoRa symbols via cyclic shifts of the reference complex chirp ( $x_0$ ) and (ii) confinement of the entire signal within the bandwidth  $B$ , conserving bandwidth.

In addition to the bandwidth and spreading factor, LoRa modulation incorporates a coding rate parameter that governs the inclusion of redundancy bits, enhancing error correction and robustness under varying channel conditions.

### A. LoRa Demodulation

To demodulate LoRa symbols, the receiver synchronizes the signal to the symbol boundary and multiplies it with the

complex conjugates of the reference chirp signal (Downchirp signal,  $\overline{x_0(t)}$ , Figure 1, middle). The resulting signal  $X_d(t)$  (Figure 1, bottom), referred to as the dechirped signal, is a complex waveform characterized by frequency  $f_m$ , phase  $\theta$  and magnitude  $A$

$$x_d(t) = \underbrace{\overline{x_0(t)} \cdot x_0(t)}_{=1} \cdot A e^{j2\pi f_m t + \theta} = A e^{j2\pi f_m t + \theta}$$

To recover the frequency offset encoding the symbol information, the receiver performs a Fast Fourier Transform (FFT) on each dechirped symbol. Sampling at rate  $F_s = B$  results in  $N = 2^{SF}$  frequency bins. The symbol  $m$  is determined by the bin with the highest magnitude. Phase  $\theta$  is discarded as it does not encode information. The received signal typically includes additive white Gaussian noise (AWGN), which distributes uniformly across bins, minimizing the likelihood of noise misleading the demodulator.

### B. Synchronization and Offset Estimation

The receiver detects a LoRa signal by identifying the preamble, consisting of consecutive reference chirps ( $x_0$ ), followed by two sync-word symbols and two and a quarter downchirps ( $\overline{x_0(t)}$ ). The receiver detects the presence of a frame upon identifying consecutive peaks from the preamble and uses the downchirp symbols with the preamble to correct the carrier frequency offset (CFO) and the sample time offset (STO).

The CFO, due to minor discrepancies between transmitter and receiver oscillator frequencies, and STO, the deviation from the actual symbol boundary, affect the frequency of the dechirped signal and FFT bin accuracy. The integer part of CFO and STO can be determined using the preamble and downchirp, but fractional components are challenging. Fractional offsets spread target bin energy across adjacent bins, complicating symbol detection in low SNR scenarios. Oversampling and fractional offset estimation techniques, such as those by Berner et al. [2], help estimate these components but do not fully resolve the issue.

### C. Effect of Collisions

In a two-packet collision, we analyze a symbol with a frequency offset  $f_m$ . The symbol boundary offset  $\Delta t$  marks the start of the interfering symbol relative to the original symbol. This results in three waveforms in the dechirped signal: a complete waveform at frequency  $f_m$ , a clipped waveform spanning from 0 and  $\Delta t$  at frequency  $f_1$  and another clipped waveform spanning from  $\Delta t$  and  $T_s$  at frequency  $f_2$ . These phenomena are illustrated in Figure 2 (left).

The spectrum of the dechirped symbol (Figure 2, right) exhibits three peaks, corresponding to the three waveforms. In cases where the colliding symbols pose comparable energy levels, the distribution of the interference symbol energy across the peaks at  $f_1$  and  $f_2$  typically preserves the target peak as the most prominent among all observed peaks. However, in scenarios where the energy of the colliding symbols exceeds the energy of the true symbol, the peaks at  $f_1$  and  $f_2$  may

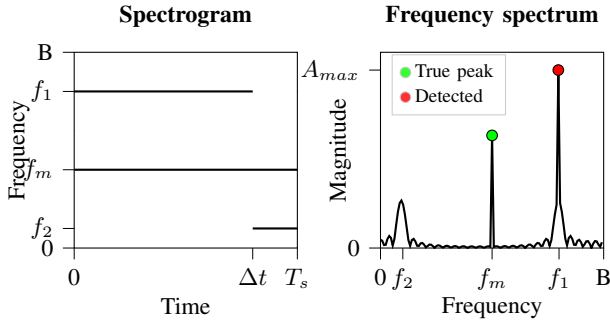


Fig. 2: Illustration of a LoRa symbol subjected to collision, showing both the spectrogram (left) and frequency spectrum (right). The baseline LoRa demodulator selects the peak at  $f_1$ , in contrast to the true peak location in  $f_m$ .

display greater energy than the true symbol, which leads to an incorrect classification of the symbol. This particular scenario is illustrated in Figure 2 (right).

#### D. Related Work

LoRa transmissions are highly susceptible to collisions [3], [4]. Several authors propose countermeasures to this problem in the context of LoRaWAN networks. Rizzi *et al.* [5] and Leonardi *et al.* [6] propose light modifications to the LoRaWAN Media Access Control, which already improve performance metrics of uplink-oriented Class-A deployments. Xu *et al.* [7] introduce an adaptive scheduling mechanism for LoRaWAN networks, that organizes devices based on their transmission patterns, with the purpose of reducing packet collisions between groups. Vincenzo *et al.* [8] improves the performance of downlink traffic for scenarios with low to medium downlink load, by improving gateway selection for downlink traffic and extending the number of gateways — at the price of increased deployment costs.

Existing work addresses the inherent constraints of LoRa transmissions through the employ of Media Access Control (MAC) strategies. Several authors propose to employ multi-hop LoRa networks to improve energy efficiency and overall communication performance [9]–[13]. There exists a growing interest in Time-Division Multiple Access schemes for LoRa communication. Zorbas *et al.* [14] propose a time-slotted scheme for LoRa traffic, which focus on applications that require frequent and very reliable communication. Haubro *et al.* [15] and Alamos *et al.* [16] design adaptations layer to facilitate the operation of TSCH and DSME modes, respectively, of IEEE 802.15.4 over the LoRa Physical Layer (PHY). Due to the nature of time-slotted communication, these strategies trade-off transmission delay with communication reliability. DSME-LoRa also enabled 6LoRa [17], a full-featured IPv6 network integration into the RIOT operating system [18].

Multiple studies [19]–[22] have examined contention-based communication in LoRa networks, targeting the facilitation of unsynchronized communication, which is a common scheme in LoRaWAN networks.

New Physical Layer (PHY) techniques have been proposed to extend the transmission range of LoRa and to enable concurrent transmissions. Li *et al.* [23] and Tesfay *et al.* [24] propose deep-learning based symbol detection to decode packets under very low SNR conditions, effectively enhancing transmission range. Over recent years, a comprehensive analysis has been carried out on multiple strategies for packet transmission within environments vulnerable to packet collisions. Eleetreby *et al.* [25] propose to unravel packet collisions in LoRaWAN by exploiting the inherent differences in carrier frequency offsets created by distinct devices. These frequency variations arise due to imperfections in crystal oscillators, a common characteristic of low-cost LoRa devices. FTrack [26] leverages both the time and frequency domain to identify the continuity of the chirp signal and eliminate interference symbols. The approach increases up to three times the network throughput at the cost of high computational complexity.

Shahid *et al.* [27] introduce the Concurrent Interference Cancellation (CIC) method that utilizes symbol boundaries to delineate sub-symbols and cancel out interference symbols by intersecting the sub-symbols spectrum. The algorithm incorporates a peak discrimination strategy, where interference peaks from incomplete cancellation are filtered out if their magnitude differs from the expected peak magnitude, which is derived from the preamble peaks. The algorithm complexity is driven by the need for the one Fast Fourier Transform (FFT) to process the dechirped symbol, in addition to two additional FFTs for each colliding packets to analyze the sub-symbols. This results in a computational complexity of  $O(N \log(N)(1 + 2K))$ , where  $N$  represents the number of data samples per symbol and  $K$  denotes the number of colliding packets. The authors have made available the original datasets along with both Matlab and Python implementations of the demodulator. Nonetheless, discrepancies arise as the implementations yield divergent outcomes when applied to the original datasets. Furthermore, the throughput results presented in the original study could not be reproduced using these tools. The Paralign [28] method conducts spectral intersection on transposed overlapping symbols to identify the actual symbols. Although this approach offers computational complexity benefits compared to previous methods, its effectiveness depends on the accurate detection of packets — a process known to be challenging in high-traffic conditions.

Tong *et al.* [29] propose CoLoRa, a method to locate peaks in a dechirped symbol even under low SNR conditions and an algorithm to group symbols by peak power ratio, in order to disentangle packet collisions. Rhati *et al.* [30] propose the TnB LoRa demodulator, which incorporates a robust frame synchronization algorithm, a symbol detector (Thrive), and a Block Error Correction (BEC) decoder algorithm. The Thrive symbol detector leverages the observation that true peaks appear as offset peaks within interference symbols, identified as siblings. Thrive calculates a matching cost to assign each demodulation window its sibling with the highest magnitude, corresponding to the fully aligned symbol. The algorithm also includes a peak history estimation to account for channel

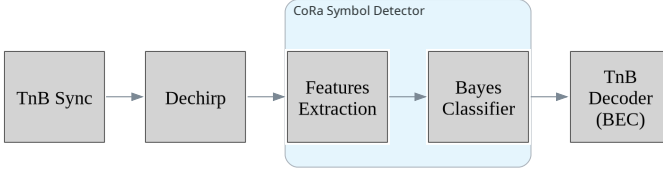


Fig. 3: System architecture of CoRa. The blue box highlights the symbol detector block, which is our main contribution

fluctuations. Unlike the Thrive algorithm, our demodulator does not require peak detection or depend on symbol boundary information. The BEC algorithm is designed to decode frames containing one or more symbol errors, significantly enhancing the decoding performance. We integrate the BEC algorithm in our work to ensure robust decoding of LoRa frames.

### III. CORA DESIGN

We design a symbol detector that employs a Bayesian classifier to estimate the value of a received symbol based on features computed directly from the dechirped symbol. This symbol detector identifies the true peak amidst interference peaks. Figure 3 illustrates our system architecture, which utilizes components of TnB [30] to leverage the synchronization and decoder blocks, but replaces the Thrive detector of TnB.

The synchronization system remains in a state of readiness for incoming frames. Upon detection of a frame, it estimates the sampling time offset and carrier frequency offset. Following the standard LoRa demodulation procedure, the system then dechirps the symbol by multiplying it with the conjugate of the base upchirp. Subsequently, the symbol detector block extracts pertinent features from the dechirped symbol, which then serve as input to the Bayesian classifier. The Bayesian classifier proceeds to select the symbol value with the highest likelihood. Following demodulation, the BEC decoder (TnB) decodes the frames. Similar to existing solutions such as CIC or TnB, the system is capable of concurrent operation.

#### A. Feature Extraction

We calculate two key features. The Peak Magnitude Deviation (PMD), which measures the discrepancy from the expected peak magnitude, and the Half-Period Discriminator (HPD), which exploits wave symmetry properties and is a novel contribution of this work.

**Peak Magnitude Deviation (PMD).** The Peak Magnitude Deviation (PMD) quantifies the difference between the observed FFT bin magnitude of a dechirped symbol and its expected peak magnitude. While CIC [27] introduces a peak filtering method based on magnitude alignment, our work builds on this principle by developing PMD as a distinct feature, applying it as a cost function to enhance peak identification under interference. We introduce the PMD, denoted as  $p_k$ , by calculating the normalized deviation of each  $X_k$  from the expected peak magnitude, capping the result at 1 to avoid extreme values.

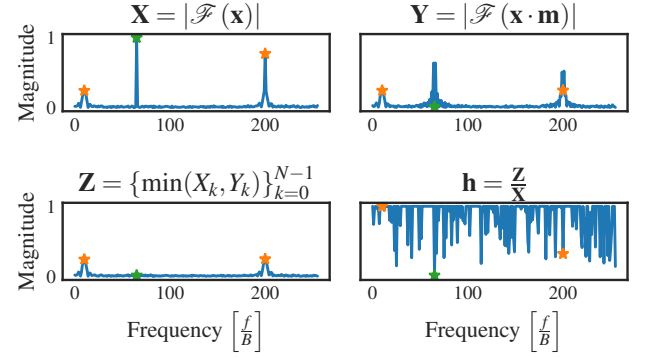


Fig. 4: Derivation of the Half-Period Discriminator (HPD), showing the spectrum of a dechirped symbol ( $X$ ), the spectrum of the signal with a phase inversion in the second half ( $Y$ ), the masked phase-inverted signal ( $Z$ ) and the output of the HPD feature. The figure shows the location of the interference peaks (orange markers) as well as the true peak (green marker)

$$\mathbf{p} = \left\{ \min \left( \left| \frac{|X_k| - E(|X_p|)}{E(X_p)} \right|, 1 \right) \right\}_{k=0}^{N-1}$$

where  $X_k$  is the dechirped symbol spectrum at bin  $k$  and  $E(X_p)$  is the expected peak magnitude.  $E(|X_p|)$  is estimated by averaging preamble peak magnitudes during synchronization.

The PMD helps assess the likelihood of a bin being the true symbol. The FFT bin containing the true peak typically aligns with the preamble peak magnitude, resulting in near-zero PMD values. Interference peaks typically produce PMD values that deviate from zero due to misalignment and clipping. Similarly, noise bins often result in PMD deviations from zero as their magnitudes are generally lower than the preamble.

While PMD serves as a useful cost function, it can misrepresent the true peak in specific scenarios: (i) At low SNR scenarios, noise can distort the true symbol energy, causing deviations that increase PMD and incorrectly penalize the true peak. (ii) When interference peaks match the preamble energy, PMD values approach zero, failing to penalize interference. To address these limitations, we introduce a second feature – the Half-Period Discriminator (HPD).

**Half-Period Discriminator (HPD).** The Half-Period Discriminator assesses the presence of symmetric or antisymmetric periodic frequency components within a signal.

This metric is built upon the observation that a true peak manifests as a complete waveform, exhibiting either symmetry (for even frequencies) or antisymmetry (for odd frequencies). In contrast, interference peaks typically appear as clipped waveforms that do not conform to symmetry patterns. This distinction aids in separating the true peak from interference peaks.

Consider a discrete signal  $\mathbf{x} = \{x_n\}_{n=0}^{N-1}$ , and a signal  $m = \{m_n\}_{n=0}^{N-1}$  defined as 1 for  $n < \frac{N}{2}$  and -1 for  $n \geq \frac{N}{2}$ .

The signal  $\mathbf{y} = \{y_n\}_{n=0}^{N-1} = \{x_n \cdot m_n\}_{n=0}^{N-1}$  then represents the discrete signal  $\mathbf{x}$  with a phase inversion in the second half of the signal. Consider the Discrete Fourier Transform of  $\mathbf{y}$ ,  $Y = \{Y_k\}_{k=0}^{N-1}$ :

$$\begin{aligned} Y_k &= \sum_{n=0}^{N-1} x_n m_n \cdot e^{-j2\pi \frac{k}{N} n} \\ &= \sum_{n=0}^{\frac{N}{2}-1} x_n e^{-j2\pi \frac{k}{N} n} - \sum_{n=\frac{N}{2}}^{N-1} x_n e^{-j2\pi \frac{k}{N} n} \\ &= \sum_{n=0}^{\frac{N}{2}-1} \left( x_n - (-1)^k x_{n+\frac{N}{2}} \right) \cdot e^{-j2\pi \frac{k}{N} n} \end{aligned} \quad (1)$$

Equation 1 shows that the symmetry of a complete waveform  $e^{j2\pi \frac{k}{N} n}$  yields  $Y_k = 0$ . In contrast, the peak of a clipped waveform attains a non-zero spectrum, as the clipped signal is neither symmetric nor antisymmetric. Figure 4 illustrates  $\mathbf{X} = |\mathcal{F}(\mathbf{x})|$ , the magnitude of the spectrum of a dechirped symbol under collisions (top left), along with  $\mathbf{Y}$ , the magnitude of the spectrum after phase inversion (top-right).

Notable, although the true peak in  $\mathbf{Y}$  exhibits energy in its neighboring components, the true peak itself yields zero, whereas other peaks show values greater than zero. We apply the minimum between the magnitude of  $\mathbf{X}$  and  $\mathbf{Y}$  to mask out the energy components around the true peak, resulting in the signal  $\mathbf{Z} = \{Z_k\}_{k=0}^{N-1} = \{\min(X_k, Y_k)\}_{k=0}^{N-1}$  (bottom-left). This signal retains energy at the interference peaks, while the values at the true peak the value remain low. We construct the HPD, denoted as  $h_k$ , by dividing  $\mathbf{Z}$  by  $\mathbf{X}$ , *i.e.*, normalizing the feature to the range  $[0, 1]$ .

$$\mathbf{h} = \frac{\mathbf{Z}}{\mathbf{X}} = \left\{ \frac{\min(|X_k|, |Y_k|)}{|X_k|} \right\}_{k=0}^{N-1}$$

As illustrated in Figure 4 (bottom-right), the HPD values at the peaks align with our previous analysis.

However, similar to PMD, HPD alone is not sufficient to reliably identify the true peak in all scenarios: (i) Noise may exhibit symmetric or antisymmetric components, resulting in HPD values close to zero. This is shown in Figure 4 (bottom-left). (ii) While carrier frequency offset (CFO) and sample time offset (STO) can be estimated and cancelled, poor estimation can cause the true peak to appear at a fractional frequency, reducing the effectiveness of phase cancellation and leading to higher HPD values.

The challenges associated with PMD and HPD are distinct and orthogonal. This motivates the development of a robust estimator that combines both features through a Bayesian Classifier to improve peak discrimination.

### B. Bayesian Classifier

Consider a dechirped symbol  $x = \{x_n\}_{n=0}^{N-1}$  obtained from a signal captured at a LoRa receiver. The spectrum of this signal exhibits three types of peaks: (i) the true peak, characterized by a complete waveform with a magnitude similar to the

preamble. (ii), interference peaks from data symbols, characterized by clipped waveforms with varying magnitude; and (iii) interference peaks from preamble symbols, characterized by two clipped waveforms with identical frequencies, which resemble a complete waveform. Since interference preamble peaks are seen as complete waveforms and may exhibit similar energy to the true peak, they can resemble the true peak. Therefore, detecting a complete waveform is insufficient for correct symbol detection. However, the position of the true peak is likely to vary across consecutive symbols due to the whitening component of the LoRa modulator, which scrambles the data and makes the data peak position independent of the previous symbol. In contrast, preamble peaks consistently arise in the same position across consecutive symbols.

Let  $T_k(\mathbf{x})$  and  $C_k(\mathbf{x})$  denotes the events that the  $k$  of the spectrum of the dechirped symbol  $x$  contain the true peak and the expected complete waveform, respectively. Let  $p_k(\mathbf{x})$  and  $h_k(\mathbf{x})$  be the values of the PMD and the HPD, respectively, of symbol  $\mathbf{x}$  at bin  $k$ . Let  $\mathbf{ph}_k(\mathbf{x}) = (p_k(\mathbf{x}), h_k(\mathbf{x}))$ . Leveraging the independence between values of consecutive data symbols, we calculate the Bayesian classifier  $P(T_k(\mathbf{x}))$  as the probability of containing the true peak at  $k$ , considering  $\mathbf{x}$  as the current symbol and  $\mathbf{x}'$  as the previous symbol. Specifically,  $T_k(\mathbf{x})$  reflects the process whereby the symbol  $\mathbf{x}$  has the true peak at  $k$  and true peak in the previous symbol appears at a different location, thereby ensuring that the peak is not a preamble peak.

$$\begin{aligned} P(T_k(\mathbf{x})) &= P(C_k(\mathbf{x}) | \mathbf{ph}_k(\mathbf{x}) \cap \neg C_k(\mathbf{x}') | \mathbf{ph}_k(\mathbf{x}')) \\ &= P(C_k(\mathbf{x}) | \mathbf{ph}_k(\mathbf{x})) \\ &\quad \cdot (1 - P(C_k(\mathbf{x}') | \mathbf{ph}_k(\mathbf{x}')))) \end{aligned} \quad (2)$$

The true peak of symbol  $\mathbf{x}$  is identified by selecting the bin  $k$  that yields the highest probability.

Utilizing Bayes's theorem, the posterior probability  $P(C_k | \mathbf{ph}_k(\mathbf{x}))$  can be estimated from the prior probability as follows:

$$P(C_k(\mathbf{x}) | \mathbf{ph}_k(\mathbf{x})) = \frac{P(\mathbf{ph}_k(\mathbf{x}) | C_k(\mathbf{x})) \cdot P(C_k(\mathbf{x}))}{P(\mathbf{ph}_k(\mathbf{x}))} \quad (3)$$

This equation indicates that by knowing the probabilities  $P(\mathbf{ph}_k(\mathbf{x}) | C_k(\mathbf{x}))$ ,  $P(C_k(\mathbf{x}))$  and  $P(\mathbf{ph}_k(\mathbf{x}))$ , we can calculate the probability of the true peak using the Bayes classifier (see Equation 2).

### C. Parameter Estimation

The posterior probability (see Equation 3), necessary for the Bayesian classifier (see Equation 2), can be determined if  $P(\mathbf{ph}_k(\mathbf{x}) | C_k(\mathbf{x}))$ ,  $P(C_k(\mathbf{x}))$ , and  $P(\mathbf{ph}_k(\mathbf{x}))$  are known. According to the law of total probability:

$$\begin{aligned} P(\mathbf{ph}_k(\mathbf{x})) &= P(\mathbf{ph}_k(\mathbf{x}) | C_k(\mathbf{x})) \cdot P(C_k(\mathbf{x})) \\ &\quad + P(\mathbf{ph}_k(\mathbf{x}) | \neg C_k(\mathbf{x})) \cdot P(\neg C_k(\mathbf{x})) \end{aligned} \quad (4)$$



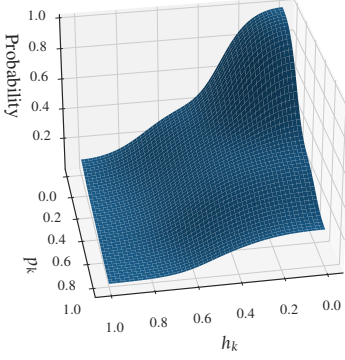


Fig. 5: Discrete (200x200 samples) posterior probability  $P[C_k(\mathbf{x}) | \mathbf{ph}_k(\mathbf{x})]$ , as a function of PMD ( $p_k$ ) and HPD ( $h_k$ ) features, estimated from simulated data. This probability is subsequently used to compute the Bayesian classifier  $P(T_k(\mathbf{x}))$ .

This reduces the problem to determining  $P(\mathbf{ph}_k(\mathbf{x}) | C_k(\mathbf{x}))$ ,  $P(\mathbf{ph}_k(\mathbf{x}) | \neg C_k(\mathbf{x}))$ , and  $P(C_k(\mathbf{x}))$ .

To estimate  $P(\mathbf{ph}_k(\mathbf{x}) | C_k)$  and  $P(\mathbf{ph}_k(\mathbf{x}) | \neg C_k)$ , we simulate samples of  $\mathbf{ph}_k$  at both the true peak and the interference or noise peaks. We then compute smoothed 2D histograms from these samples to calculate the discrete probabilities.

The probability  $P(C_k)$  is derived from the ratio of the true peak samples to the total number of samples.

To create the true peak and interference/noise sample sets, we extract  $\mathbf{ph}_k$  samples from 100,000 dechirped symbols, each containing 256 bins. Each symbol comprises a complete waveform (which represent the true peak) and up to two interference packets, each characterized by two clipped waveforms, which are uniformly distributed in terms of their frequencies and positions. Transmission power is uniformly distributed between -15 dB and 13 dB. To account for synchronization errors, a small fractional frequency deviation, uniformly distributed within  $\pm \frac{1}{8}$  of the Nyquist frequency, is added to the symbol frequency.

For robust estimation, we focus on challenging symbols misclassified by the baseline LoRa demodulator, for which the true peak magnitude is not the most prominent. The true peak set comprises the  $p_k$  and  $h_k$  features of the bin containing the true peak. The interference set includes the 10 samples of  $\mathbf{ph}_k$  feature pairs with the lowest Peak Magnitude Deviation ( $p_k$ ), ensuring the Bayesian classifier emphasizes the HPD feature ( $h_k$ ) for accurate classification.

By using the expressions for the discrete probabilities and the total probability, we obtain the discrete probability  $P[C_k | \mathbf{ph}_k]$  depicted in Figure 5. As anticipated, low values of  $p_k$  and  $h_k$ , which characterize the true peak, yield high probabilities. Conversely, high values of  $p_k$  and  $h_k$ , which are indicative of noise or interference peaks, result in low probabilities.

The posterior probability can be evaluated using interpolation techniques such as nearest neighbor or linear interpolation. For memory constrained devices, function approximations such as spline interpolation are feasible.

Using the evaluated posterior probability in Equation 2, we derive the Bayes classifier.

#### IV. EVALUATION

We now evaluate the performance of our proposed demodulator in comparison to the standard LoRa receiver (baseline), and the two state-of-the-art demodulators CIC and TnB. We utilize the CIC demodulator and the baseline implementation from OpenLoRa [31]. For TnB, we use the reference MATLAB implementation [30]. Our demodulator is implemented in *Python* using the *NumPy* library. To integrate the synchronization and decoding blocks of TnB, we interface our solution with TnB by employing the MATLAB Engine API [32]. The posterior probability (see Figure 5), used to evaluate the Bayesian classifier, is implemented using nearest neighbor interpolation with a grid of 200x200 samples. This grid maps the calculated HPD and PMD values to the closest value in the discrete probability estimated from simulated data. This method ensures the accuracy of the classifier while maintaining computational efficiency. We conduct the evaluation on a *Quad-Core Intel Core i7-8650U* Linux machine running at 1.9GHz with 16GB of RAM.

To foster a fair comparison, we conduct the analysis on the two datasets provisioned by the related work. Both datasets contain real-world LoRa signals of fixed transmitter devices. The first dataset (from CIC) includes four scenarios with varying SNR conditions and fixed PHY parameters. The second dataset (from TnB) comprises three scenarios with varying SNR conditions and varying PHY parameters. The characteristics of these datasets, as well as the transmission parameters, are summarized in Table I. All captures involve 20 transmitter devices, each sending a 12-byte payload.

##### A. Collision Resolution

Figure 6 depicts the throughput of the baseline, CIC, TnB, and the CoRa demodulator using the CIC dataset. The CoRa approach demonstrates superior throughput in all scenarios, achieving up to 29% improvement over TnB in high SNR conditions without Line-of-Sight (see Figure 6, D2 at 95 pkt/s) and up to a 6% improvement in the Sub-Noise SNR scenario (see Figure 6, D4 at 100 pkt/s). Given that our demodulator utilizes the synchronization and decoding blocks of TnB, the observed performance difference is attributed to the superior efficacy of our demodulator over the Thrive demodulator utilized in TnB. Correspondingly, our solutions exhibits up to a 178% improvement over CIC and delivers up to 11.53 times higher throughput than the baseline in high SNR conditions (see Figure 6, left, 100 pkt/s).

Consistently, TnB shows better results than CIC for two main reasons. (i) the effectiveness of CIC decreases with frame collisions, in which symbol boundaries are closer than 10% of the symbol time – a situation that occurs in approximately 20%

Parameter	CIC Dataset				TnB Dataset		
	D1	D2	D3	D4	Indoor	Outdoor1	Outdoor2
Spreading Factor			8			8, 10	
Bandwidth [kHz]			250			125	
Coding Rate			4/5			4/5, 4/6, 4/7, 4/8	
Sampling Rate [MHz]			2			1	
SNR (SF8) [dB]	30 to 42	30 to 42	10 to 30	-17 to 5	-5 to 17	-10 to 10	-8 to 14
SNR (SF10) [dB]			-		-9 to 23	-17 to 12	-13 to 12
Deployment area [m <sup>2</sup> ]	15 × 10	100 × 60	170 × 100	1200 × 1600	100 × 120	400 × 240	220 × 200
TX Rate [pkt/s]			5 to 100			20, 25	
Capture Time [s]			60			30	

TABLE I: Configuration parameters of LoRa devices across captured scenarios

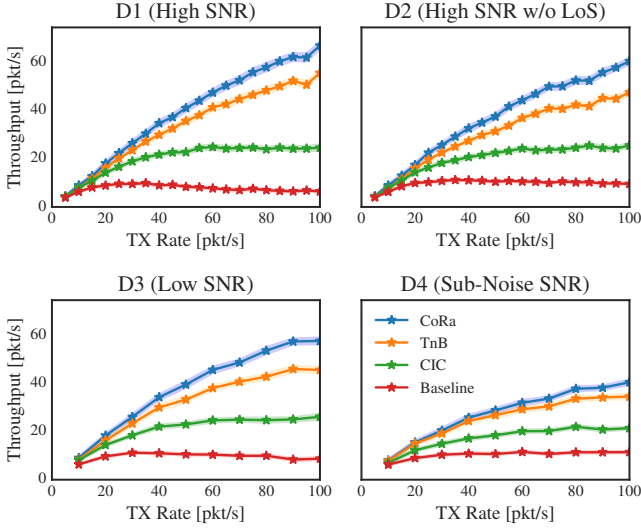


Fig. 6: Throughput vs aggregated transmission rate in the CIC dataset. The shaded areas around the curves indicate the error margins.

of the collisions. (ii) the correction capabilities of the BEC scheme utilized by TnB is superior to those of the standard LoRa decoding scheme.

For the baseline, performance deteriorates significantly with an increased aggregated transmission ratio and a decrease in Signal-to-Noise Ratio (SNR). This is mainly due to the synchronization procedure of the standard demodulator, which identifies the preamble by detecting consecutive symbols of identical value. Frequent frame collisions in combination with low SNR can corrupt the demodulated values, thereby hindering accurate frame detection. In contrast, the frame detection methods of CIC and TnB remain effective even under frame collisions and increase their throughput.

For the TnB dataset (see Figure 7), the CoRa demodulator performs comparably to or better than TnB. It shows significantly enhanced performance in scenarios with high SNR and lower spreading factor (SF), achieving up to 24% higher throughput than TnB (indoor, SF8, CR4/6).

A decrease in SNR, as experienced in the outdoor scenarios (SF8, left-center and left-bottom), degrades the estimation of

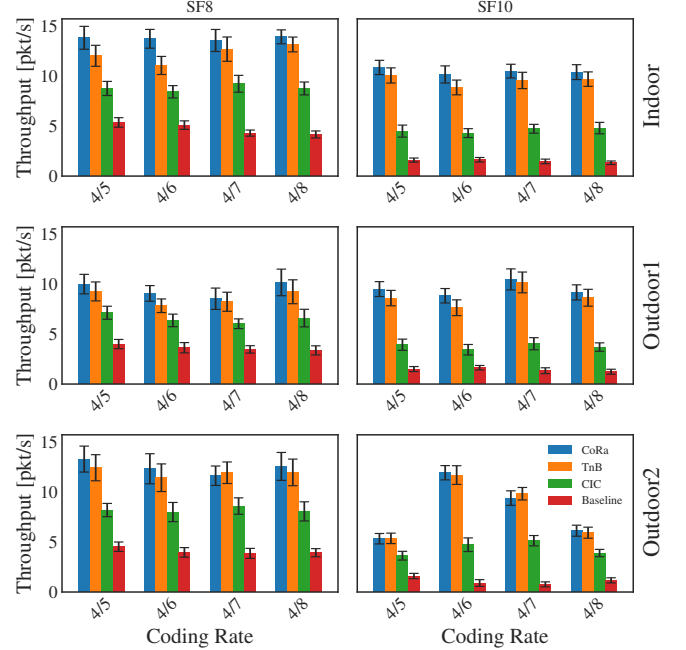


Fig. 7: Throughput vs coding rate in the TnB dataset. Devices with spreading factor 10 and coding rates 4/5 and 4/8 transmit 20 pkt/s, while devices in all other scenarios transmit 25 pkt/s.

the Bayesian classifier features due to increased noise. This results in lower throughput and reduces the gap between CoRa and TnB, as seen in Outdoor1 (15% improvement over TnB at CR 4/6) and Outdoor2 (7% improvement over TnB at CR 4/6). For CR4/7 and CR4/8 in the Outdoor1 and Outdoor2 scenarios (SF8, left), TnB and our demodulator perform statistically comparable.

In the SF 10 scenarios (see Figure 7, right), our solution shows a smaller performance advantage than for the SF8 scenarios, with an average improvement of 9% in the Indoor scenario and 8% in the Outdoor1 scenario. In the CR4/7 case in Outdoor1 (SF10, right), as well as for all Outdoor2 scenarios (SF10, right), TnB and CoRa perform statistically comparable. Note that in the Outdoor2 scenario (SF10, right), the CR4/5 and CR4/8 scenarios have notably less throughput due to the capture scenario with a transmission rate of only 20 packets

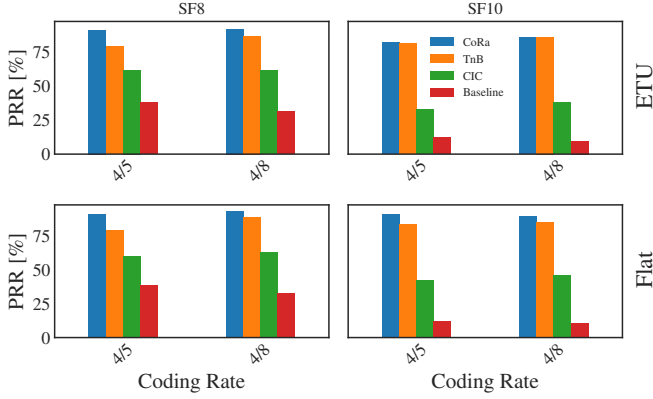


Fig. 8: Packet Reception Ratio vs. coding rate in the simulated dataset for LTE Extended Typical Urban (ETU) and Flat channels. Devices transmit at 15 pkt/s with SF8 (SNR:  $[-5, 15]$  dB) and SF10 (SNR:  $[-10, 10]$  dB), using a 125 kHz bandwidth.

per second.

These results confirm that while CIC always outperforms the baseline, it still falls short compare to TnB and our solution. The baseline achieves a maximum of 5 packets per second in the SF8 scenario (indoor, CR4/5) and up to 1.5 packets per second in the SF10 scenario (outdoor1, CR4/6). In contrast, our approach exhibits an average throughput improvement of  $2.2\times$  compared to the CIC demodulator and  $7.4\times$  compared to the Baseline.

### B. Resistance to Multipath Fading and Doppler Effect

The real-world captures of the CIC and TnB datasets do not account for mobility nor environments notably affected by multi-path fading, which are common in dense urban areas. To evaluate the robustness of our solution in such conditions, we continue with simulated packet traces from an LTE Extended Typical Urban (ETU) channel model [33]. This model is characterized by strong fluctuations and multi-path fading. Specifically, the channel is defined by a Power Delay Profile (PDP) with 9 taps, each undergoing Rayleigh fading. The channel also features delay spread of  $5\mu\text{s}$  and a maximum Doppler shift of  $5\text{Hz}$ .

We generate simulated captures of 900 LoRa transmissions using *NumPy*. These simulations include scenarios with both the ETU channel and a flat channel, the latter of which does not incorporate multi-path fading or Doppler shift.

Figure 8 presents the packet reception ratio for the evaluated demodulators. In the SF8 scenario under the ETU channel conditions (top-left), our demodulator outperforms the current state-of-the-art solutions, despite the strong channel fluctuations. Specifically, our demodulator improves the packet reception ratio over TnB by approximately 12.3% with a coding rate of 4/5 and by about 5% with a coding rate of 4/8. In the SF10 scenario (top-right in the figure), both the CoRa and the TnB demodulators perform similarly, with less than one percent difference.

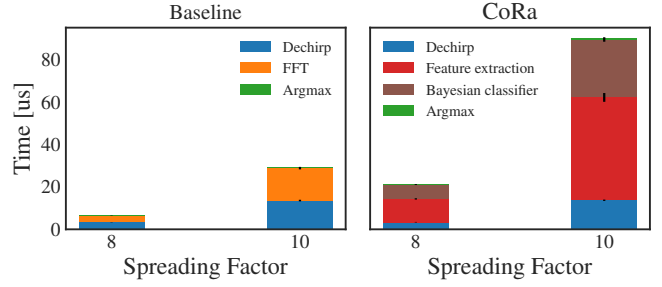


Fig. 9: Execution time per symbol for standard LoRa (Baseline) and CoRa demodulators at SF8 and SF10, showing stage-wise contribution to total demodulation time.

When comparing the variations of packet reception ratios between the ETU and flat channels, we observe that the TnB algorithm and the baseline are more robust against channel fluctuations. The TnB decoder varies only around 2% between ETU and flat channels, while the baseline shows a variation of about one percent. In contrast, the CIC and the CoRa demodulator are more affected by strong fluctuations, as illustrated in the SF10 scenarios (Figure 8, top-right and bottom-right). Specifically, in the ETU channel, the packet reception ratio for CIC and CoRa demodulator decreases by 9 resp. 8 percentage points, with a coding rate of 4/5, and by 8 resp. 4 points at the coding rate 4/8.

### C. Performance Overhead

We observe from Figure 9 that the CoRa demodulator spends approximately 50% of the time on feature extraction, where the primary load is the calculation of two Fast Fourier Transforms (FFTs). This operation is computationally efficient with a complexity of  $O(N\log N)$ . Approximately 30% of the time is spent on the Bayesian classifier, which includes the index calculation ( $O(N)$ ) and the evaluation in the grid ( $O(1)$ ). The dechirping procedure, which includes applying the carrier frequency offset corrections from the synchronization algorithm, accounts for around 15% of the time. The Argmax operation ( $O(N)$ ), which identifies the bin with the highest probability of being the true peak, is negligible in terms of computational time.

Thus, the overall complexity of our demodulator is  $O(N\log N)$ , primarily dictated by the feature extraction stage. In comparison to the equally complex Baseline demodulator we observe a constant overhead factor of approximately 3 – regardless of the spreading factor.

## V. DISCUSSION

### Which are the main advantages of the CoRa demodulator?

The evaluation results provide compelling evidence that the CoRa demodulator is capable of successfully demodulating frames, even under conditions of severe collisions and significant channel variations, as well as in mobile scenarios.

The CoRa symbol detector offers the following advantages over existing work. First, it does not rely on peak detection,



which is prone to errors, particularly in environments with low Signal-to-Noise Ratio (SNR). Furthermore, our demodulator operates independently of symbol boundary information. This characteristic enables the demodulation of symbols without the need to wait for the frame synchronization of the next incoming frame. In related work, a symbol is impacted by an incoming frame, because of which the demodulator may be unable to determine whether it is a colliding frame unless it waits for detecting this next symbol, which requires tracking up to 12.25 symbols (comprising 8 preamble symbols, 2 Start Frame Delimiter (SFD) symbols and 2.25 downchirp symbols). This not only increases latency, as the demodulator cannot immediately classify the symbol without the necessary symbol boundary information, but also escalates implementation complexity by necessitating the monitoring of pending symbols and awaiting the subsequent frame.

Moreover, the independence from symbol boundary information enhances the versatility of our symbol detector across various scenarios. One such scenario is Frequency Hop Spreading Spectrum (FHSS), where the LoRa transceiver transmit packet fragments across multiple channels. This feature is standard in LoRa devices and should not be confused with LR-FHSS, which employs GMSK modulation and narrowband signals. Another scenario involves accurately detecting symbols even if the frame synchronization mechanism fails to detect colliding frames. In case of FHSS, when the frequency hopping pattern is unknown – such as when independent LoRa networks transmit data simultaneously – it becomes impossible to predict potential symbol collisions since symbols may appear on different channels. This limitation renders certain algorithms ineffective, such as TnB or CoLoRa, which are designed to match peaks to transmitting devices.

**Can CoRa Process Packets in Real-time?** The analysis presented in Section IV-C indicates that the CoRa demodulator exhibits a constant overhead of approximately 3 times over the baseline LoRa demodulator. The computational complexity of our solution is  $O(N \log N)$ , dominated by the complexity of the Fast Fourier Transform (FFT). Consider for example a Digital Signal Processor (DSP) operating at 200 MHz, which requires 25 cycles per point for computation of the FFT. In a scenario with  $N = 256$  samples (spreading factor 8, bandwidth 125 KHz) the time required for the FFT is calculated as follows:

$$T_{256} = \frac{25 \cdot 256 \cdot \mu s}{200,000,000} = 32 \mu s$$

Given that the symbol time in this scenario is  $T_s = 1.024$  ms, and assuming the demodulator spends half of the time on FFTs (see Figure 9), the total time spend on demodulation is approximately  $64 \mu s$ . This duration represents roughly 6% of the total symbol time. Hence, the CoRa complexity in packet processing does not challenge real-time.

Our demodulator exhibits significantly lower computational complexity than the CIC symbol detector, which requires  $(1 + 2K)$  Fast Fourier Transforms (FFTs) per colliding symbol, where  $K$  is the number of detected colliding frames. Hence,

the complexity of CIC increases polynomially with the number of collisions, whereas our solution remains constant.

The Thrive (TnB) algorithm involves three main computational steps: FFT calculation ( $O(N \log N)$ ), peak detection ( $O(N)$ ), and peak cost evaluations ( $O(N)$ ). These peak cost evaluations are performed up to  $2M^2$  times per symbol, where  $M$  denotes the number of colliding packets within the symbol. Since  $M \ll N$ , where  $N$  denotes the number of samples per symbol, the overall complexity of Thrive simplifies to  $O(N \log N)$ , aligning with our solution, where the FFT step dominates the total computational cost. Still, the runtime of TnB cost evaluations scales quadratically, leading to unbounded execution time. In our solution, the runtime remains constant.

## VI. CONCLUSIONS AND OUTLOOK

In this study, we introduced the CoRa symbol detector, engineered to accurately identify LoRa symbols even under conditions of severe collisions. Our methodology utilized a Bayesian classifier to discern the true symbol peak amidst the peaks from colliding symbols within the spectrum of the dechirped signal. The foundation of CoRa lies in harnessing the symmetry properties of a complete waveform, identified as the true peak, and the observation that the magnitude of the true peak remains relatively constant within a frame. This approach facilitates the calculation of robust features, ultimately enabling the precise identification of the true peak within the dechirped symbol.

We replaced the symbol detector of a state-of-the-art method (TnB) to develop a robust LoRa demodulator. This demodulator underwent rigorous evaluations with comparison against recent state-of-the-art demodulators and the baseline LoRa demodulator. The assessment utilized both real-world and simulated data to comprehensively evaluate its efficacy and performance.

Results indicated that our approach yields outcomes that are either superior or at least comparable with those of the state-of-the-art solutions, even under conditions of sub-noise Signal-to-Noise Ratio (SNR). The performance advantage of CoRa is particularly evident in scenarios characterized by extreme collisions. Notably, our solution maintains a constant overhead, specifically three times the demodulation times of the baseline LoRa demodulator. This suggests the potential feasibility of the implementation on real hardware.

The present study opens two future research directions. First, further research should refine the feature calculation to account for channel fluctuations, which holds promise for boosting symbol detection performance in scenarios with strong multipath fading or Doppler effect. Second, implementing and deploying CoRa on a Software Defined Radio (SDR) will facilitate a comprehensive evaluation in more complex real-world scenarios.

**Artifacts.** The authors have provided public access to their code and data at <https://doi.org/10.5281/zenodo.14582713>

# REFERENCES

- [1] M. I. Hossain and J. I. Markendahl, "Comparison of LPWAN Technologies: Cost Structure and Scalability," *Wireless Personal Communications*, vol. 121, no. 1, pp. 887–903, 2021.
- [2] C. Bernier, F. Dehmas, and N. Deparis, "Low complexity lora frame synchronization for ultra-low power software-defined radios," *IEEE Transactions on Communications*, vol. 68, no. 5, pp. 3140–3152, 2020.
- [3] G. Ferre, "Collision and packet loss analysis in a LoRaWAN network," in *25th European Signal Processing Conference (EUSIPCO'17)*. Piscataway, NJ, USA: IEEE, 2017, pp. 2586–2590.
- [4] C. Orfanidis, L. M. Feeney, M. Jacobsson, and P. Gunningberg, "Cross-Technology Clear Channel Assessment for Low-Power Wide Area Networks," in *16th International Conference on Mobile Ad Hoc and Sensor Systems (MASS'19)*. Washington, DC, USA: IEEE Computer Society, 2019, pp. 199–207.
- [5] M. Rizzi, P. Ferrari, A. Flammini, E. Sisinni, and M. Gidlund, "Using LoRa for industrial wireless networks," in *13th International Workshop on Factory Communication Systems (WFCS'17)*. Piscataway, NJ, USA: IEEE Press, 2017, pp. 1–4.
- [6] L. Leonardi, L. L. Bello, F. Battaglia, and G. Patti, "Comparative Assessment of the LoRaWAN Medium Access Control Protocols for IoT: Does Listen before Talk Perform Better than ALOHA?" *Electronics*, vol. 9, no. 4, p. 553, 2020.
- [7] Z. Xu, J. Luo, Z. Yin, T. He, and F. Dong, "S-mac: Achieving high scalability via adaptive scheduling in lpwan," in *IEEE INFOCOM 2020 - IEEE Conference on Computer Communications*, 2020, pp. 506–515.
- [8] V. D. Vincenzo, M. Heusse, and B. Tourancheau, "Improving Downlink Scalability in LoRaWAN," in *IEEE International Conference on Communications (ICC'19)*. Piscataway, NJ, USA: IEEE, 2019.
- [9] J. R. Cotrim and J. ao Henrique Kleinschmidt, "LoRaWAN Mesh Networks: A Review and Classification of Multihop Communication," *Sensors*, vol. 20, no. 15, p. 4273, 2020.
- [10] B. Sartori, S. Thielemans, M. Bezunartea, A. Braeken, and K. Steenhaut, "Enabling RPL multihop communications based on LoRa," in *13th International Conference on Wireless and Mobile Computing, Networking and Communications (WiMob '17)*. Washington, DC, USA: IEEE Computer Society, 2017, pp. 1–8.
- [11] S. Thielemans, M. Bezunartea, and K. Steenhaut, "Establishing transparent IPv6 communication on LoRa based low power wide area networks (LPWANS)," in *Wireless Telecommunications Symposium (WTS '17)*. Piscataway, NJ, USA: IEEE, 2017, pp. 1–6.
- [12] A. Abrardo and A. Pozzebon, "A Multi-Hop LoRa Linear Sensor Network for the Monitoring of Underground Environments: The Case of the Medieval Aqueducts in Siena, Italy," *Sensors*, vol. 19, no. 2, p. 402, 2019.
- [13] M. Bezunartea, R. V. Glabbeek, A. Braeken, J. Tiberghien, and K. Steenhaut, "Towards Energy Efficient LoRa Multihop Networks," in *International Symposium on Local and Metropolitan Area Networks (LANMAN '19)*. Piscataway, NJ, USA: IEEE, 2019, pp. 1–3.
- [14] D. Zorbas, K. Abdelfadeel, P. Kotzanikolaou, and D. Pesch, "TS-LoRa: Time-slotted LoRaWAN for the Industrial Internet of Things," *Computer Communications*, vol. 153, pp. 1–10, 2020.
- [15] M. Haubro, C. Orfanidis, G. Oikonomou, and X. Fafoutis, "TSCH-over-LoRa: long range and reliable IPv6 multi-hop networks for the internet of things," *Internet Technology Letters*, vol. 3, no. 4, p. e165, 2020.
- [16] J. Alamos, P. Kietzmann, T. C. Schmidt, and M. Wählisch, "DSME-LoRa: Seamless Long Range Communication Between Arbitrary Nodes in the Constrained IoT," *Transactions on Sensor Networks (TOSN)*, vol. 18, no. 4, pp. 1–43, November 2022. [Online]. Available: <https://dl.acm.org/doi/10.1145/3552432>
- [17] J. Alamos, T. C. Schmidt, and M. Wählisch, "6LoRa: Full Stack IPv6 Networking with DSME-LoRa on Low Power IoT Nodes," in *Proc. of Embedded Wireless Systems and Networks (EWSN'23)*. New York, USA: ACM, September 2023, pp. 145–150. [Online]. Available: <https://dl.acm.org/doi/10.5555/3639940.3639960>
- [18] E. Baccelli, C. Gündogan, O. Hahm, P. Kietzmann, M. Lenders, H. Petersen, K. Schleiser, T. C. Schmidt, and M. Wählisch, "RIOT: an Open Source Operating System for Low-end Embedded Devices in the IoT," *IEEE Internet of Things Journal*, vol. 5, no. 6, pp. 4428–4440, December 2018. [Online]. Available: <http://doi.org/10.1109/JIOT.2018.2815038>
- [19] A. Gamage, J. C. Liando, C. Gu, R. Tan, and M. Li, *LMAC: Efficient Carrier-Sense Multiple Access for LoRa*. New York, NY, USA: Association for Computing Machinery, 2020. [Online]. Available: <https://doi.org/10.1145/3372224.3419200>
- [20] C. Pham, "Investigating and experimenting CSMA channel access mechanisms for LoRa IoT networks," in *Wireless Communications and Networking Conference (WCNC '18)*. Piscataway, NJ, USA: IEEE, 2018, pp. 1–6.
- [21] M. O'Kennedy, T. Niesler, R. Wolhuter, and N. Mitton, "Practical evaluation of carrier sensing for a LoRa wildlife monitoring network," in *Proc. of 19th IFIP Networking Conference*. Piscataway, NJ, USA: IEEE Press, June 2020, pp. 10–18.
- [22] R. M. Liaqat, P. Branch, and J. But, "A novel approach to collision avoidance in lora networks," in *2023 Fourteenth International Conference on Ubiquitous and Future Networks (ICUFN)*, 2023, pp. 412–417.
- [23] C. Li, H. Guo, S. Tong, X. Zeng, Z. Cao, M. Zhang, Q. Yan, L. Xiao, J. Wang, and Y. Liu, "Nelora: Towards ultra-low snr lora communication with neural-enhanced demodulation," in *Proceedings of the 19th ACM Conference on Embedded Networked Sensor Systems*, ser. SenSys '21. New York, NY, USA: Association for Computing Machinery, 2021, p. 56–68. [Online]. Available: <https://doi.org/10.1145/3485730.3485928>
- [24] A. A. Tesfay, E. P. Simon, S. Kharbech, and L. Clavier, "Deep learning-based signal detection for uplink in lora-like networks," in *2021 IEEE 32nd Annual International Symposium on Personal, Indoor and Mobile Radio Communications (PIMRC)*, 2021, pp. 617–621.
- [25] R. Eleteby, D. Zhang, S. Kumar, and O. Yağan, "Empowering low-power wide area networks in urban settings," in *Proceedings of the Conference of the ACM Special Interest Group on Data Communication*, ser. SIGCOMM '17. New York, NY, USA: Association for Computing Machinery, 2017, p. 309–321. [Online]. Available: <https://doi.org/10.1145/3098822.3098845>
- [26] X. Xia, Y. Zheng, and T. Gu, "Ftrack: Parallel decoding for lora transmissions," in *Proceedings of the 17th Conference on Embedded Networked Sensor Systems*, ser. SenSys '19. New York, NY, USA: Association for Computing Machinery, 2019, p. 192–204. [Online]. Available: <https://doi.org/10.1145/3356250.3360024>
- [27] M. O. Shahid, M. Philipose, K. Chintalapudi, S. Banerjee, and B. Krishnaswamy, "Concurrent interference cancellation: Decoding multi-packet collisions in lora," in *Proceedings of the 2021 ACM SIGCOMM 2021 Conference*, ser. SIGCOMM '21. New York, NY, USA: Association for Computing Machinery, 2021, pp. 503–515. [Online]. Available: <https://doi.org/10.1145/3452296.3472931>
- [28] Y. Wang, F. Zhang, X. Zheng, L. Liu, and H. Ma, "Decoding LoRa Collisions via Parallel Alignment," *ACM ToSN*, vol. 19, no. 3, mar 2023.
- [29] S. Tong, Z. Xu, and J. Wang, "Colora: Enabling multi-packet reception in lora," in *IEEE INFOCOM 2020 - IEEE Conference on Computer Communications*. IEEE Press, 2020, p. 2303–2311.
- [30] R. Rathi and Z. Zhang, "TnB: resolving collisions in LoRa based on the peak matching cost and block error correction," in *Proc. of the 18th Intern. Conf. on Emerging Networking Experiments and Technologies*, ser. CoNEXT '22. New York, NY, USA: ACM, 2022, p. 401–416.
- [31] M. Mishra, D. Koch, M. O. Shahid, B. Krishnaswamy, K. Chintalapudi, and S. Banerjee, "OpenLoRa: Validating LoRa implementations through an extensible and open-sourced framework," in *20th USENIX Symposium on Networked Systems Design and Implementation (NSDI 23)*. Boston, MA: USENIX Association, Apr. 2023, pp. 1165–1183. [Online]. Available: <https://www.usenix.org/conference/nsdi23/presentation/mishra>
- [32] The MathWorks, Inc., "MATLAB Engine for Python," The MathWorks, Inc., 2024, accessed: 2024-07-29. [Online]. Available: <https://www.mathworks.com/help/matlab/matlab-engine-for-python.html>
- [33] 3rd Generation Partnership Project (3GPP), "Technical Report 36.873: Study on 3D channel model for LTE," 3rd Generation Partnership Project (3GPP), Tech. Rep. TR 36.873 V12.7.0, 2017, accessed: 2024-07-29. [Online]. Available: [https://www.3gpp.org/ftp/Specs/archive/36\\_series/36.873/36873-e70.zip](https://www.3gpp.org/ftp/Specs/archive/36_series/36.873/36873-e70.zip)